Check for updates

RESEARCH ARTICLE

ADVANCED MATERIALS INTERFACES

www.advmatinterfaces.de

Highly Homogeneous 2D/3D Heterojunction Diodes by Pulsed Laser Deposition of MoS_2 on Ion Implantation Doped 4H-SiC

Filippo Giannazzo, Salvatore Ethan Panasci, Emanuela Schilirò, Patrick Fiorenza, Giuseppe Greco, Fabrizio Roccaforte, Marco Cannas, Simonpietro Agnello, Antal Koos, Béla Pécz, Marianna Španková, and Štefan Chromik*

In this paper, 2D/3D heterojunction diodes have been fabricated by pulsed laser deposition (PLD) of MoS_2 on 4H-SiC(0001) surfaces with different doping levels, i.e., n^- epitaxial doping (≈10^{16} cm^{-3}) and n^+ ion implantation doping (>10^{19} cm^{-3}). After assessing the excellent thickness uniformity (≈3L-MoS_2) and conformal coverage of the PLD-grown films by Raman mapping and transmission electron microscopy, the current injection across the heterojunctions is investigated by temperature-dependent current–voltage characterization of the diodes and by nanoscale current mapping with conductive atomic force microscopy. A wide tunability of the transport properties is shown by the SiC surface doping, with highly rectifying behavior for the MoS_2/n^- SiC junction and a strongly enhanced current injection for MoS_2/n^+ SiC one. Thermionic emission is found the dominant mechanism ruling forward current in MoS_2/n^- SiC diodes, with an effective barrier $\Phi_B = (1.04 \pm 0.09)$ eV. Instead, the significantly lower effective barrier $\Phi_B = (0.31 \pm 0.01)$ eV and a temperature-dependent ideality factor for MoS_2/n^+ SiC junctions is explained by thermionic-field-emission through the thin depletion region of n^+ doped SiC. The scalability of PLD MoS_2 deposition and the electronic transport tunability by implantation doping of SiC represents key steps for industrial development of MoS_2/SiC devices.

1. Introduction

Layered transition metal dichalcogenides (TMDs), including MoS_2, WS_2, $MoSe_2$, WSe_2, have been widely investigated in the last years, due to their interesting semiconducting properties, such as the thickness-dependent bandgap, which are attractive for ultra-scaled digital electronics beyond silicon, optoelectronics, and energy applications.[1] The dangling-bond free structure of TMDs offers the unique possibility of realizing high-quality van der Waals heterostructures with bulk semiconductors for the implementation of advanced heterojunction devices exploiting current transport at the interface.[2–5] In particular, the integration of single or few layers MoS_2 with wide bandgap semiconductors, such as the group-III Nitrides (GaN, AlN, and AlGaN alloys) and 4H-SiC, is currently the object of increasing interest in optoelectronics (e.g., for the realization of high responsivity dual-band photodetectors covering the spectral ranges of visible and ultraviolet),[6–11] and in electronics (e.g., for the realization of heterojunction diodes, including band-to-band tunnel diodes).[12–17]

Motivated by these interests, different approaches have been employed to fabricate such heterojunction devices, including the transfer of MoS_2 flakes exfoliated from bulk crystals[6,9,10] or grown on foreign substrates,[12,13,18] and the direct deposition of MoS_2 on GaN[14–16] or 4H-SiC.[11,17] In particular, nearly unstrained and highly oriented monolayer MoS_2 triangular domains on the GaN(0001) basal plane have been

F. Giannazzo, S. E. Panasci, E. Schilirò, P. Fiorenza, G. Greco, F. Roccaforte, S. Agnello
CNR-IMM
Strada VIII, Catania 5 95121, Italy
E-mail: filippo.giannazzo@imm.cnr.it

S. E. Panasci
Department of Physics and Astronomy
University of Catania
Via Santa Sofia 64, Catania 95123, Italy

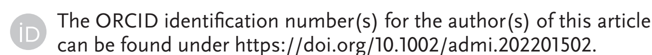
The ORCID identification number(s) for the author(s) of this article can be found under https://doi.org/10.1002/admi.202201502.

© 2022 The Authors. Advanced Materials Interfaces published by Wiley-VCH GmbH. This is an open access article under the terms of the Creative Commons Attribution License, which permits use, distribution and reproduction in any medium, provided the original work is properly cited.

DOI: 10.1002/admi.202201502

M. Cannas, S. Agnello
Department of Physics and Chemistry Emilio Segré
University of Palermo
Via Archirafi 36, Palermo 90143, Italy

S. Agnello
AtenCenter
University of Palermo
Viale delle Scienze Ed.18, Palermo 90128, Italy

A. Koos, B. Pécz
Centre for Energy Research
Institute of Technical Physics and Materials Science
Konkoly-Thege ut 29–33, Budapest 1121, Hungary

M. Španková, Š. Chromik
Institute of Electrical Engineering SAS
Dúbravská cesta 9, Bratislava 84104, Slovakia

© 2022 The Authors. Advanced Materials Interfaces published by Wiley-VCH GmbH

21967350, 0, Downloaded from https://onlinelibrary.wiley.com/doi/10.1002/admi.202201502 by Cochrane Hungary, Wiley Online Library on [04/01/2023]. See the Terms and Conditions (https://onlinelibrary.wiley.com/terms-and-conditions) on Wiley Online Library for rules of use; OA articles are governed by the applicable Creative Commons License

obtained by chemical vapor deposition (CVD) at a temperature of 700–800 °C.[14,19,20] Epitaxial MoS_2 growth on GaN has been also obtained by the pulsed laser deposition (PLD) technique.[21] The high-quality epitaxial growth has been ascribed to the very low (<1%) in-plane lattice mismatch between the MoS_2 and GaN hexagonal lattices, and to the similar thermal expansion coefficients of the two materials.

On the other hand, the larger lattice constants mismatch (≈2.9%, with a_{MoS2} = 3.162 Å and a_{4H-SiC} = 3.073 Å)[22] and the difference in thermal expansion coefficients ($\alpha_{MoS2} = 1.90 \times 10^{-6}$ K^{-1}, $\alpha_{4H-SiC} = 4.47 \times 10^{-6}$ K^{-1})[23,24] between MoS_2 and 4H-SiC may contribute to interfacial strain. To date, few layers or monolayer MoS_2 films uniformly covering the SiC(0001) surface have been reported by CVD approaches, i.e., the single-step CVD with vapors from S and MoO_3 powders[11] or the sulfurization of predeposited Mo thin films.[17] Highly crystalline few layers MoS_2 on 6H-SiC(0001) have been also obtained by PLD at a substrate temperature of 700 °C.[21] Furthermore, inhomogeneous MoS_2 flakes with dendritic shape,[25] or vertically standing triangular MoS_2 domains with respect to the basal planes of 6H-SiC[26] and 4H-SiC[27] have been obtained by CVD properly tailoring the growth conditions. While vertically standing MoS_2 exposing edges can be interesting for catalysis and hydrogen evolution reaction (HER) applications,[27] layered MoS_2 films uniformly covering the SiC(0001) basal plane are highly attractive as building blocks of heterojunction devices exploiting vertical current transport at MoS_2/SiC interfaces. These can find application both in the state-of-the-art 4H-SiC technology (Schottky and Junction Barrier Schottky diodes) for energy-efficient power conversion,[28] as well as for the implementation of novel device concepts for ultra-fast switching, including p^+-MoS_2/n^+-SiC Esaki diodes[29] and vertical hot electron transistors with a n-MoS_2 base[30,31] and n^+-SiC emitter. Besides the reported studies, a more comprehensive understanding of the structural properties and of the mechanisms ruling current transport across MoS_2/SiC interfaces is mandatory for the future development of these heterojunction devices. However, to date, only a few studies reported on the electronic transport in MoS_2/SiC diodes, mainly focused on anisotype (p/n) junctions of p^+ MoS_2 with n^+ 4H-SiC,[12,29] whereas there is a lack of knowledge on the isotype (n/n) MoS_2/4H-SiC heterojunctions.

In this paper, the PLD technique has been employed to deposit highly uniform ≈3L-MoS_2 films on the surface of 4H-SiC(0001) samples with different n-type doping levels, i.e., low n-type doping (10^{16} cm^{-3}) epitaxy and degenerate n-type doping (>10^{19} cm^{-3}) by phosphorous ion implantation. After assessing the MoS_2 thickness uniformity and the structural properties of the heterojunction by Raman mapping combined with atomic resolution transmission electron microscopy (TEM), the electronic transport mechanisms at the interfaces have been deeply investigated both on macroscopic diodes and at nanoscale by conductive atomic force microscopy (C-AFM) current mapping.[32,33] A wide tunability of current injection at the hetero-interfaces by the near-surface doping of SiC is demonstrated, showing a highly rectifying behavior on n^- 4H-SiC and strongly enhanced current injection on n^+- implanted 4H-SiC. Furthermore, the mechanisms ruling current injection under forwarding bias polarization (i.e., thermionic emission above the MoS_2/SiC conduction band discontinuity for n^- 4H-SiC and thermionic field emission across the ultra-thin depletion region of SiC for n^+ 4H-SiC) have been discussed based on the results of temperature-dependent current-voltage (I–V) characterization of diodes and C-AFM nanoscale current mapping.

2. Experimental Section

Two 4H-SiC(0001) samples with different n-type surface doping have been used for the MoS_2 PLD growth experiments. They were prepared from the same initial 4H-SiC (0001) 4°-off wafer, consisting of a n^+ substrate covered by a 5 µm moderately n-type doped epitaxial layer, with a carrier concentration of ≈1 × 10^{16} cm^{-3} evaluated by Hg-probe capacitance measurements. The first sample (from now on named n^--SiC sample) was a 10 mm × 10 mm piece cut from this wafer. For the second sample (from now on named n^+-SiC sample), phosphorous (P) ions implantation at energies from 30 to 200 keV and doses from 7.5 × 10^{13} to 5 × 10^{14} cm^{-2} was performed at a temperature of 400 °C, followed by activation annealing at 1675 °C in Ar ambient. These implant and annealing conditions resulted in a n^+ doping profile, with an active donors concentration ≈1 × 10^{19} cm^{-3} in the near surface region and a concentration plateau of ≈(8.5–9) × 10^{19} cm^{-3} in the depth range from 90 to 170 nm.[34,35] The phosphorous doping concentration profile, measured by secondary ions mass spectrometry (SIMS), and the active donor's concentration, evaluated by scanning capacitance microscopy on cross-sectioned samples, are illustrated in Figure S1, Supporting Information.[34]

Ultra-thin films of MoS_2 have been grown on the two different 4H-SiC samples by PLD with a MBE/PLD-2000 system equipped a 248 nm wavelength KrF excimer laser Compex 102, and using a target of MoS_2. Two-inch diameter commercial stoichiometric MoS_2 target rotated at the speed of 6 rpm. The substrates (10 × 10 mm^2) were placed on the rotating holder 10 cm away from the target. The deposition temperature was about 700 °C. After the deposition, the temperature was decreased at a rate of 50 °C min^{-1} until 200 °C, and then by natural cooling. The KrF excimer laser operated at a 4 Hz pulse rate. The energy pulse was 60–70 mJ and the laser spot size was 2 mm^2. The total number of the pulses to achieve the deposition of 3–4L MoS_2 typically ranges from 330–380 pulses. The exact number depends on the state of the MoS_2 target at the starting of the deposition, the accuracy of pulse energy, and the substrate position on the rotating heater. A preliminary calibration was performed immediately before the deposition on the 4H-SiC substrates. Based on this calibration, a number of 380 pulses was used in this experiment to achieve the desired MoS_2 thickness.

The thickness uniformity of MoS_2 was evaluated by Raman spectroscopy and mapping on different areas of the samples, using a Horiba HR-Evolution micro-Raman system with a confocal microscope (100× objective) and a laser excitation wavelength of 532 nm. All the spectra have been calibrated using the E_2(TA) vibrational peak of 4H-SiC (at 204 cm^{-1}) as reference. Furthermore, high-resolution transmission electron microscopy (HR-TEM) and energy dispersion spectroscopy (EDS) analyses of the cross-sectioned MoS_2/SiC samples (lamellas preparation with focused ion beam) were carried out with an aberration-corrected Thermofisher Themis 200 microscope. The current injection at the interface between the PLD-grown MoS_2 and 4H-SiC was

© 2022 The Authors. Advanced Materials Interfaces published by Wiley-VCH GmbH

21967350, 0, Downloaded from https://onlinelibrary.wiley.com/doi/10.1002/admi.202201502 by Cochrane Hungary, Wiley Online Library on [04/01/2023]. See the Terms and Conditions (https://onlinelibrary.wiley.com/terms-and-conditions) on Wiley Online Library for rules of use; OA articles are governed by the applicable Creative Commons License

21967350, 0, Downloaded from https://onlinelibrary.wiley.com/doi/10.1002/admi.202201502 by Cochrane Hungary, Wiley Online Library on [04/01/2023]. See the Terms and Conditions (https://onlinelibrary.wiley.com/terms-and-conditions) on Wiley Online Library for rules of use; OA articles are governed by the applicable Creative Commons License

probed at nanoscale by conductive atomic force microscopy (C-AFM) with a DI3100 system by Bruker with Nanoscope V electronics. The sample's surface was scanned with Pt-coated Si tips (with curvature radius $r_{tip} \approx 5$ nm) to simultaneously collect morphology and current maps, while applying a potential difference between the tip and the samples' backside. Furthermore, local *I–V* curves were acquired on arrays of tip positions on the samples' surface. Finally, macroscopic circular contacts with 100 µm radius were lithographically fabricated on both the n^- SiC and n^+ SiC by deposition of a Ni(20 nm)/Au(80 nm) metal stack, followed by resist lift-off. Temperature-dependent *I–V* characterization of the resulting metal/MoS_2/SiC heterojunction diodes was carried out using a Karl Suss Microtec probe station equipped with a HP4156B parameter analyzer.

3. Results and Discussion

The as-deposited MoS_2 films were initially investigated by Raman mapping on different sample areas, in order to evaluate the MoS_2 thickness uniformity. Two representative Raman spectra collected on the MoS_2/n^--SiC surface (blue line) and on the MoS_2/n^+- SiC one (red line) are reported in **Figure 1**a. The most prominent features in the spectral range from 150 to 500 cm^{-1} are represented by the E_2(TA) mode at 204 cm^{-1} associated to 4H-SiC substrate, and the two first-order MoS_2 vibrational modes (E_{2g} and A_{1g}) between 370 and 420 cm^{-1}. In particular, measuring the wavenumber difference ($\Delta\omega = \omega_{A_{1g}} - \omega_{E_{2g}}$) between these two characteristic Raman peaks is commonly taken as a straightforward way to evaluate the number of MoS_2 layers.[36] The thickness uniformity of the PLD-grown MoS_2 films was determined by statistical analysis on arrays of 144 Raman spectra collected on 10 µm × 10 µm areas. Figure 1b,c shows the color maps of the $\Delta\omega$ values extracted from the arrays measured on the MoS_2/n^--SiC and MoS_2/n^+-SiC samples, respectively. The number of MoS_2 layers corresponding to the $\Delta\omega$ values are also indicated in the color bar in the lowest part of Figure 1c. Furthermore, the histograms of the $\Delta\omega$ values extracted from the two color maps are reported in Figure 1d, showing very narrow distributions with the maximum values and standard deviations of 24.02 ±0.07 cm^{-1} and 23.58 ± 0.13 cm^{-1} for the MoS_2 on n^--type 4H-SiC (blue histogram) and n^+ 4H-SiC (red histogram),

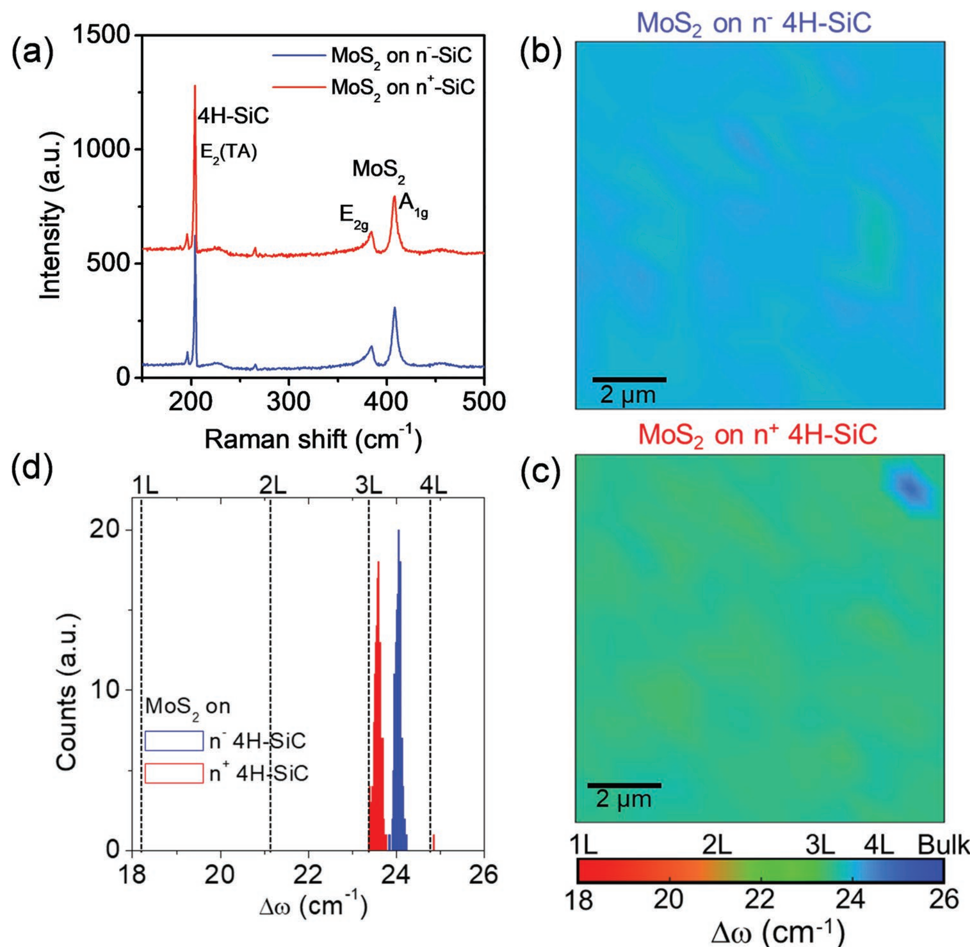

Figure 1. a) Typical Raman spectra of PLD grown MoS_2 on n^--SiC (blue line) and on n^+-SiC (red line), showing the E_2(TA) peak belonging to the 4H-SiC substrate and the two characteristics in-plane (E_{2g}) and out-of plane (A_{1g}) vibrational modes of MoS_2. Color maps of the A_{1g} and E_{2g} wavenumber differences $\Delta\omega = \omega_{A_{1g}} - \omega_{E_{2g}}$ evaluated from an array of 144 Raman spectra collected on 10 µm ×10 µm areas of the MoS_2/n^--SiC b) and MoS_2/n^+-SiC c) samples. The number of MoS_2 layers associated with the $\Delta\omega$ value is indicated in the color scale. d) Histograms of the $\Delta\omega$ values associated with the two color maps, showing a very uniform thickness distribution (from 3 to 4 layers) of MoS_2 on the two samples.

© 2022 The Authors. Advanced Materials Interfaces published by Wiley-VCH GmbH

21967350, 0, Downloaded from https://onlinelibrary.wiley.com/doi/10.1002/admi.202201502 by Cochrane Hungary, Wiley Online Library on [04/01/2023]. See the Terms and Conditions (https://onlinelibrary.wiley.com/terms-and-conditions) on Wiley Online Library for rules of use; OA articles are governed by the applicable Creative Commons License

respectively. These statistical analyses, performed at different positions of the two 10 mm × 10 mm samples, indicate a very uniform ≈3L MoS_2 coverage on the n^+ 4H-SiC surface and ≈3.5L coverage on the n^- 4H-SiC one.

In addition to the thickness uniformity, Raman mapping provided interesting information on the strain status of the as-grown MoS_2 films. In particular, the measured $\omega_{E_{2g}}$ values are known to be very sensitive to the local biaxial strain (ε) induced by the interaction of MoS_2 membranes with the substrate, according to the relation:

$$\omega_{E_{2g}} = \omega_{E_{2g}^0} - 2\gamma_{E_{2g}}\omega_{E_{2g}^0}\varepsilon \quad (1)$$

where $\omega_{E_{2g}^0}$ = 382.9 cm^{-1} is the E_{2g} wavenumber for a suspended (i.e., unstrained) 3L MoS_2 membrane, while $\gamma_{E_{2g}} = 0.39$ is the value of the Grüneisen parameter for 3L MoS_2.[37] Figure S2a–c, Supporting Information shows the color maps and the histograms of the experimental $\omega_{E_{2g}}$ values extracted from the arrays of Raman spectra on the MoS_2/n^--SiC and MoS_2/n^+-SiC samples. From these distributions and according to Equation (1), we estimated similar compressive strain values of –0.34 ± 0.02% and –0.39 ± 0.04% for MoS_2 on the n^--type 4H-SiC and on n^+-4H-SiC, respectively.

The position of the A_{1g} peak is known to be sensitive to the interaction of the MoS_2 membrane with the substrate, specifically to the doping induced by charge transfer phenomena.[38] Figure S2d–f, Supporting Information shows the color maps and the histograms of the A_{1g} wavenumbers obtained from arrays of 144 Raman spectra collected on 10 µm ×10 µm areas of the MoS_2/n^--SiC and MoS_2/n^+-SiC samples. The very narrow distributions of the A_{1g} wavenumbers indicate very uniform doping of MoS_2 membranes.

The structural properties of the MoS_2 heterojunctions with the 4°-off-axis 4H-SiC (0001) crystals have been further investigated by TEM analyses on cross-sectioned samples. **Figure 2**a,b are two representative high-resolution TEM images for PLD-grown MoS_2 on the unimplanted n^- 4H-SiC epitaxy and on the n^+-implanted 4H-SiC. In both cases, the MoS_2 films exhibit a uniform thickness and follow in a conformal way the characteristic steps of 4H-SiC surface due to the wafer 4°-off miscut angle. Looking more in detail at the number of MoS_2 layers, the presence of 3L-4L regions can be observed on the n^- 4H-SiC sample (Figure 2a), whereas a more uniform 3L thickness is evident for the n^+ doped 4H-SiC surface, consistently with the results of Raman statistics. The presence of a very thin (≈1.4–1.5 nm) amorphous film at the interface between MoS_2 and SiC is also observed in the two samples. EDS chemical mapping, reported in Figure S3, Supporting Information, indicated that its composition is SiO_2. Furthermore, the two TEM analyses in Figure 2a,b confirm a very good crystalline quality of 4H-SiC in the near interface region, even in the case of the n^+-implanted sample. This is due to the lower phosphorus concentration (≈10^{19} cm^{-3}) in the near surface region of the implanted profile (see the SIMS in Figure S1, Supporting Information). On the other hand, the presence of implant-related defects in the 4H-SiC lattice at higher depths (from ≈90 to ≈170 nm), implanted with a P concentration of 10^{20} cm^{-3} can be observed in low magnification TEM analyses, shown in Figure S4, Supporting information. As it will be evident in the following, a comparable crystalline quality of 4H-SiC in the near interface region is important for the interpretation of electrical transport properties of MoS_2/SiC heterojunctions.

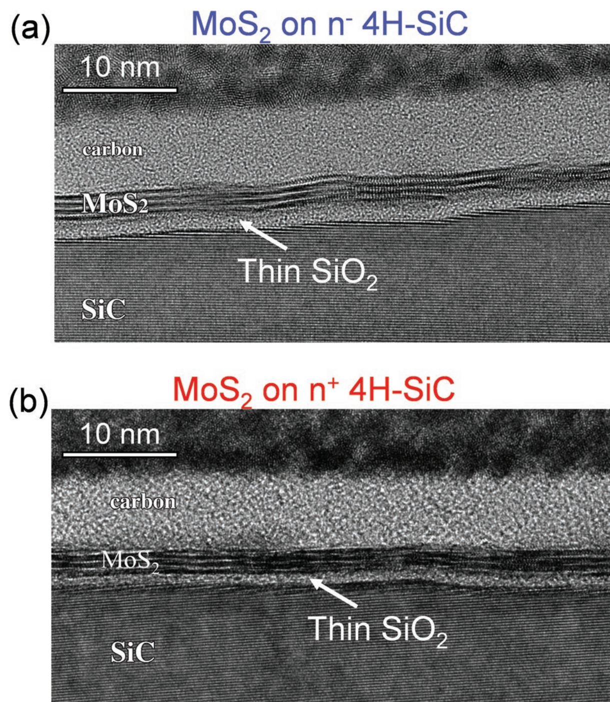

Figure 2. Cross-sectional high-resolution TEM images of MoS_2 on a) n^--4H-SiC and on b) n^+ implanted 4H-SiC.

After this preliminary structural characterization, the current injection at the heterojunctions between the ultra-thin MoS_2 films and 4H-SiC with different surface doping has been investigated by current-voltage characterization of vertical diode structures, schematically illustrated in the inserts of **Figure 3**a,b. Two typical current density (J) versus bias characteristics measured at room temperature (T = 300 K) on the two samples are reported in Figure 3a,b. The MoS_2 junction with the moderately n-doped 4H-SiC (Figure 3a) exhibits an excellent rectifying behavior, with extremely low current density under reverse bias polarization (J_{rev} ≈ 7.5 × 10^{-8} A cm^{-2} at –10 V), the exponential growth of the J–V characteristic under forward polarization (J_{fw} ≈ 20 A cm^{-2} at +3 V, limited by series resistance) and a resulting rectification ratio I_{fw}/I_{rev} ≈ 10^8. On the other hand, a strongly enhanced current injection across the junction is observed for MoS_2 thin films grown on the degenerately n^+ doped 4H-SiC surface (Figure 3b), thus demonstrating the possibility of tailoring the vertical electronic transport by ion-implantation doping of the wide bandgap semiconductor. It is worth mentioning that the electrical characterization of Ni contacts on n^- 4H-SiC and on n^+ 4H-SiC (implanted under identical conditions to those used in the present work) have been reported by Vivona et al.,[35] showing similar qualitative behavior the I–V characteristics but different values of the ideality factors and barrier heights.

To get a deeper insight on the physical mechanisms ruling current injection at the two heterojunctions, we performed a temperature-dependent electrical characterization of the diodes. **Figure 4**a,b shows the forward bias characteristics on the two

© 2022 The Authors. Advanced Materials Interfaces published by Wiley-VCH GmbH

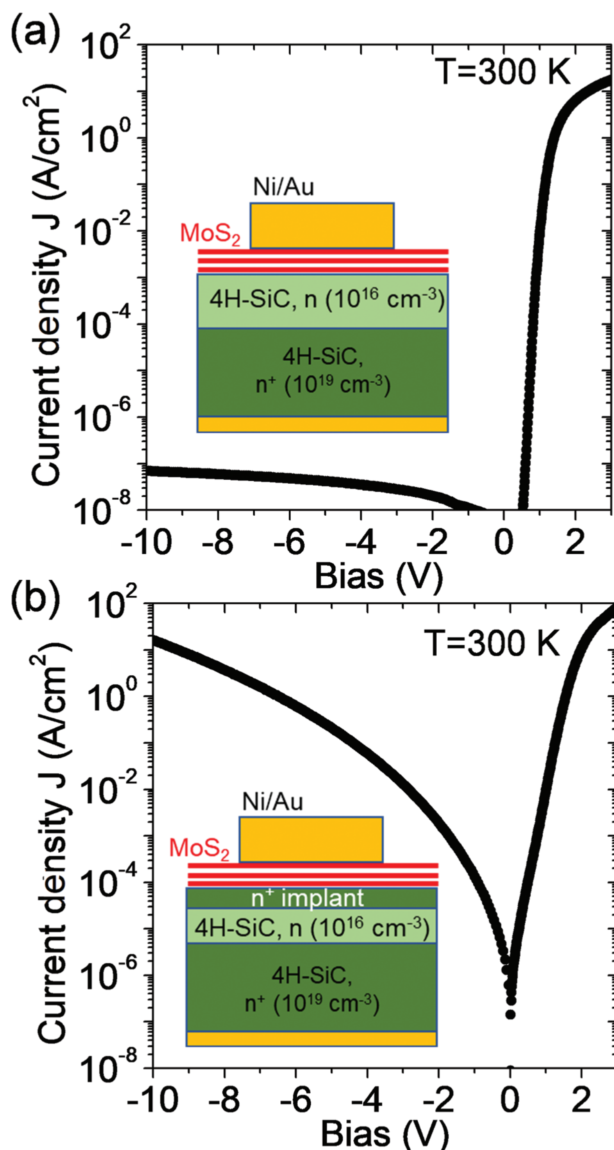

Figure 3. Current density-voltage characteristics of MoS_2 heterojunction diodes on a) n^- – doped and b) n^+-implanted 4H-SiC collected at room temperature (T = 300 K). Schematic illustrations of the vertical diodes structure with Ni/Au top contact and backside contacts are reported in the insert of panels (a) and (b).

samples collected at different temperatures from 300 to 400 K. An increase of the current density J with T is observed in both cases, indicating the occurrence of temperature-activated electronic transport above/through an energy barrier, such as thermionic emission or thermionic field emission. The schematic band diagrams of the $MoS_2/SiO_2/n^-$-SiC and $MoS_2/SiO_2/n^+$-SiC heterojunctions are reported in the inserts of Figure 4a,b, respectively, where the band alignments have been estimated considering the literature values of energy bandgap and electron affinities for few-layers MoS_2, SiO_2 and 4H-SiC.[39] Unintentional n-type doping of MoS_2 (as typically reported in the literature for MoS_2 produced by different methods) is considered for both heterojunctions, whereas n^- and degenerate n^+ doping of 4H-SiC is accounted in the two cases. Due to the presence of the ultra-thin SiO_2 interfacial layer, the J–V characteristics of the junctions can be described, in a first approximation, with a modified thermionic emission equation:[40]

$$J = J_s e^{\frac{qV}{nk_BT}} \tag{2}$$

where q is the electron charge, k_B is the Boltzmann constant, n is the ideality factor, and the term J_s is expressed as:

$$J_s = A^* P_t T^2 e^{-\frac{q\Phi_B}{k_BT}} \tag{3}$$

being A^* the Richardson constant of 4H-SiC,[41] Φ_B the heterojunction barrier between MoS_2 and 4H-SiC, and P_t the direct tunneling probability across the ultra-thin SiO_2 barrier. This latter term is expected to be temperature-independent and can be expressed as $P_t = \exp\left[-\frac{4\pi\delta\sqrt{2m_{ox}\psi}}{h}\right]$, being $\psi \approx 2.7$ eV the SiO_2/4H-SiC conduction band discontinuity,[42] $\delta \approx 1.4$ nm the thickness of the SiO_2 layer evaluated by TEM, m_{ox} the direct tunneling effective mass of SiO_2 [43] and h the Planck's constant.

The current density term J_s and the ideality factor n for the two groups of J–V characteristics in Figure 4a,b were obtained by fitting the linear region of each semilog curve with Equation (2) and taking the intercept and the slope, respectively. After evaluating the J_s terms at the different measurement temperatures T, the Arrhenius plots of the $\ln[J_s/T^2]$ versus 1000/T for the two heterojunction diodes have been built and reported in Figure 4c. According to Equation (3), the effective barrier height values for MoS_2 on n^- 4H-SiC ($\Phi_B = 1.04 \pm 0.09$ eV) and n^+ 4H-SiC ($\Phi_B = 0.31 \pm 0.01$ eV) are obtained by the slopes of these plots. Furthermore, the dependence of the ideality factor n on the temperature T for the two heterojunction diodes is reported in Figure 4d.

Noteworthy, the experimentally determined energy barrier $\Phi_B = (1.04 \pm 0.09)$ eV for the MoS_2 diode on the 4H-SiC epitaxy is very close to the value of the MoS_2/SiC conduction band discontinuity $\Delta E_C = \chi_{MoS_2} - \chi_{4H-SiC} \approx 1eV$, where χ_{MoS_2} and χ_{4H-SiC} are the literature values of the electron affinities of the two semiconductors.[38,44] Furthermore, as shown in Figure 4d this diode exhibits an ideality factor $n \approx 1.25$, nearly independent on the measuring temperature T. According to the classical Card & Rhoderick model for metal-insulator-semiconductor tunnel junctions,[45] the slight departure of n from unity can be ascribed to the presence of traps states located at the interface between the thin SiO_2 layer and 4H-SiC, as expressed in the following equation:

$$n = 1 + \frac{qD_{it}\delta}{\varepsilon_0\varepsilon_{ox}} \tag{4}$$

where ε_0 is the vacuum dielectric constant, ε_{ox} = 3.9 the SiO_2 relative permittivity, $\delta \approx 1.4$ nm the SiO_2 thickness, and D_{it} the interface traps density. By fitting the T-independent n behavior in Figure 4d with Equation (4), a $D_{it} \approx 4 \times 10^{12}$ cm^{-2} eV^{-1} has been evaluated, which can be associated to carbon residues present in the nanometer SiO_2 film due to 4H-SiC oxidation.

© 2022 The Authors. Advanced Materials Interfaces published by Wiley-VCH GmbH

21967350, 0, Downloaded from https://onlinelibrary.wiley.com/doi/10.1002/admi.202201502 by Cochrane Hungary, Wiley Online Library on [04/01/2023]. See the Terms and Conditions (https://onlinelibrary.wiley.com/terms-and-conditions) on Wiley Online Library for rules of use; OA articles are governed by the applicable Creative Commons License

21967350, 0, Downloaded from https://onlinelibrary.wiley.com/doi/10.1002/admi.202201502 by Cochrane Hungary, Wiley Online Library on [04/01/2023]. See the Terms and Conditions (https://onlinelibrary.wiley.com/terms-and-conditions) on Wiley Online Library for rules of use; OA articles are governed by the applicable Creative Commons License

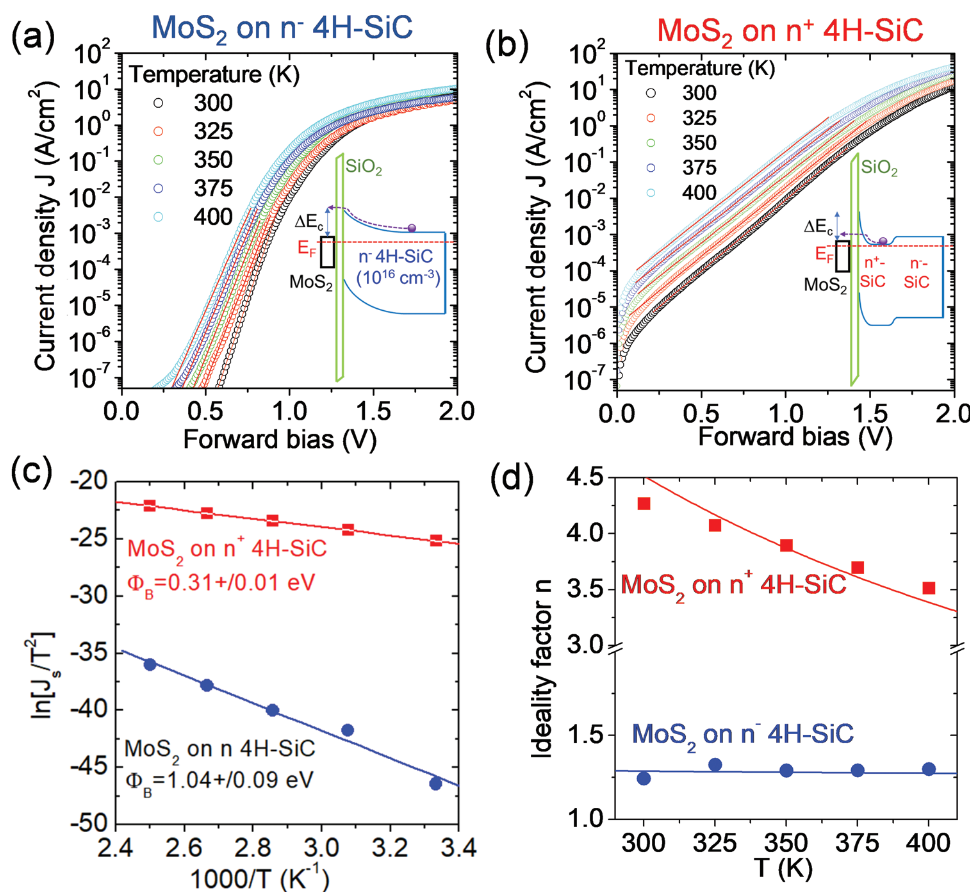

Figure 4. Forward bias current density–voltage (J–V) characteristics at different temperatures (from 300 to 400 K) for the MoS_2 diodes on n^--4H-SiC (a) and on n^+ implanted 4H-SiC (b). The open circles represent the experimental data, whereas the red lines are the fits of the linear regions of the semilog J–V curves. c) Arrhenius plots of $\ln[J_s/T^2]$ versus 1000/T for the two diodes and evaluation of the effective heterojunctions barrier heights from the slopes of the liner fits. d) Ideality factor n versus the measurement temperature for the two heterojunctions. The blue line is the fit of the T-independent n-values for the $MoS_2/SiO_2/n^-$4H-SiC junction using the Card&Rhoderick model, whereas the red line is the fit of the n dependence on T considering the TFE model. The schematic band diagrams of the two $MoS_2/SiO_2/SiC$ heterojunctions with an ultra-thin SiO_2 tunneling barrier are reported in the inserts of (a) and (b), with the illustration of the different current injection mechanisms deduced from the temperature-dependent electrical characterization.

The ideality factor close to unity and the good matching of the experimental barrier height Φ_B with the MoS_2/SiC conduction band discontinuity ΔE_c confirms that thermionic emission above the barrier is the dominant current injection mechanism in MoS_2 diodes on n^- 4H-SiC, as schematically illustrated in the insert of Figure 4a. On the other hand, the results in Figure 4d, e show that, for MoS_2 diodes on n^+ 4H-SiC, the evaluated effective barrier height (Φ_B = 031 ± 0.01 eV) is much lower than ΔE_c, while the ideality factor n strongly deviates from unity with a significant temperature dependence. The reduced effective barrier height indicates the tunneling of thermally excited electrons through the ultrathin depletion region of n^+-doped 4H-SiC (as schematically depicted in the insert of Figure 4b), i.e., the occurrence of a thermionic field emission (TFE) mechanism. This mechanism is further supported by the temperature dependence of n. In fact, the current-voltage curves in the TFE processes can be expressed as:

$$J_{\mathrm{TFE}} = J_{\mathrm{s,TFE}}\, e^{\frac{qV}{E_0}} \tag{5}$$

where the voltage dependence is formally identical to the one for TE (Equation (1)), by expressing the characteristic energy E_0 as $E_0 = nk_BT/q$. From this analogy, the temperature dependence of the ideality factor determined in Figure 4d can be described as[46]:

$$n = \frac{qE_0}{k_BT} = \frac{qE_{00}}{k_BT}\coth\left(\frac{qE_{00}}{k_BT}\right) \tag{6}$$

where the energy E_{00} depends on the surface donors concentration N_D of n^+ doped 4H-SiC as[35,45]:

$$E_{00} = \frac{h}{\pi}\sqrt{\frac{N_D}{m_{\mathrm{eff,SiC}}\varepsilon_0\varepsilon_{\mathrm{SiC}}}} \tag{7}$$

being $m_{\mathrm{eff,SiC}}$ = 0.42 m_0 the effective mass and $\varepsilon_{\mathrm{SiC}}$ = 9.6 the relative permittivity of 4H-SiC, respectively. By fitting the temperature dependence of n on T for MoS_2 diodes on n^+-SiC with Equations (6)–(7), as shown in Figure 4d, a value of $N_D \approx 1 \times 10^{19}$ cm^{-3} is obtained. This is consistent with the active donors concentration in the surface region of implanted

© 2022 The Authors. Advanced Materials Interfaces published by Wiley-VCH GmbH

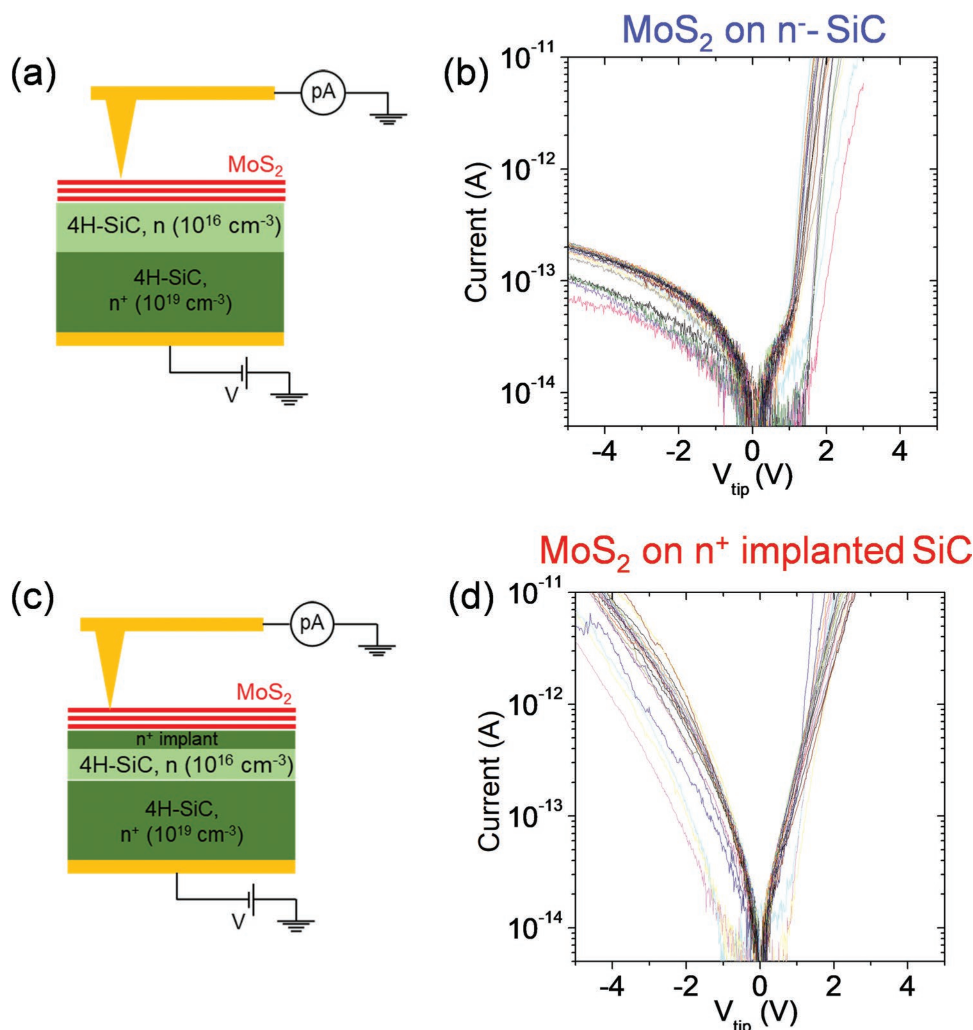

Figure 5. Schematic illustrations of the C-AFM setup for nanoscale resolution *I–V* characterization and current mapping on MoS_2 heterojunctions with n^- (a) and n^+-implanted 4H-SiC (c). Local I-V_{tip} characteristics collected on arrays of 5 × 5 tip positions on MoS_2 on n^--SiC (b) and MoS_2 on n^+-SiC (d).

4H-SiC, as illustrated in the profiles reported in Figure S1, Supporting Information. Furthermore, the high crystalline quality of the near-surface region of n^+-implanted 4H-SiC, demonstrated by TEM analyses in Figure 2b, allows to exclude other transport mechanisms, such as tunneling mediated by implant-related defects in the n^+-SiC depletion region.

The above-discussed temperature-dependent electrical analyses provide information on the average current injection behavior over the areas of macroscopic contacts (with 100 µm radius). However, probing the local homogeneity of current transport down to nanometer scale is crucial, both to get a deeper insight on the electrical quality of the PLD-grown MoS_2 on 4H-SiC and in the perspective of realizing scaled or nanostructured devices. To this aim, local current–voltage (*I–V*) measurements and current mapping have been carried out directly on the as-deposited few-layer MoS_2 on n^- and n^+ -doped 4H-SiC, using a Pt-coated Si tip as a nanoscale electrical contact, as schematically depicted in **Figure 5**a,c. Two representative sets of *I–*V_{tip} curves collected by displacing the tip over two arrays of 5 × 5 positions (with 1 µm spacing) on the surface of the two samples are reported in Figure 5b,d, respectively. All the local *I–V* characteristics for MoS_2 on n^--4H-SiC exhibit a strongly rectifying behavior, whereas a significantly enhanced conduction under negative polarization is observed for MoS_2 on n^+-implanted 4H-SiC.

The local barrier heights for the MoS_2/SiC heterojunctions have been evaluated from the forward bias *I–*V_{tip} collected by C-AFM, by properly adapting the thermionic emission model (Equations (2) and (3)) to the nanoscale system. **Figure 6**a schematically illustrates the Pt tip/MoS_2/SiC heterojunction and the equivalent circuit, consisting in the series combination of different contributions, i.e., the tip resistance (R_{tip}), the Pt/MoS_2 nano-contact resistance ($R_{C,nano}$), the MoS_2/SiC diode, the spreading resistance (R_{spr}) of the locally injected current in the SiC bulk crystal, the drift resistance (R_d) of bulk SiC and the macroscopic back-contact resistance ($R_{C,macro}$). In particular, the R_{tip}, R_d, and $R_{C,macro}$ are constant terms independent of the tip position, whereas $R_{C,nano}$ depends on the local electrical properties of MoS_2 (i.e., the Pt/MoS_2 Schottky barrier and MoS_2 doping) and R_{spr} on the local resistivity of 4H-SiC.

© 2022 The Authors. Advanced Materials Interfaces published by Wiley-VCH GmbH

21967350, 0, Downloaded from https://onlinelibrary.wiley.com/doi/10.1002/admi.202201502 by Cochrane Hungary, Wiley Online Library on [04/01/2023]. See the Terms and Conditions (https://onlinelibrary.wiley.com/terms-and-conditions) on Wiley Online Library for rules of use; OA articles are governed by the applicable Creative Commons License

ADVANCED MATERIALS INTERFACES
www.advmatinterfaces.de

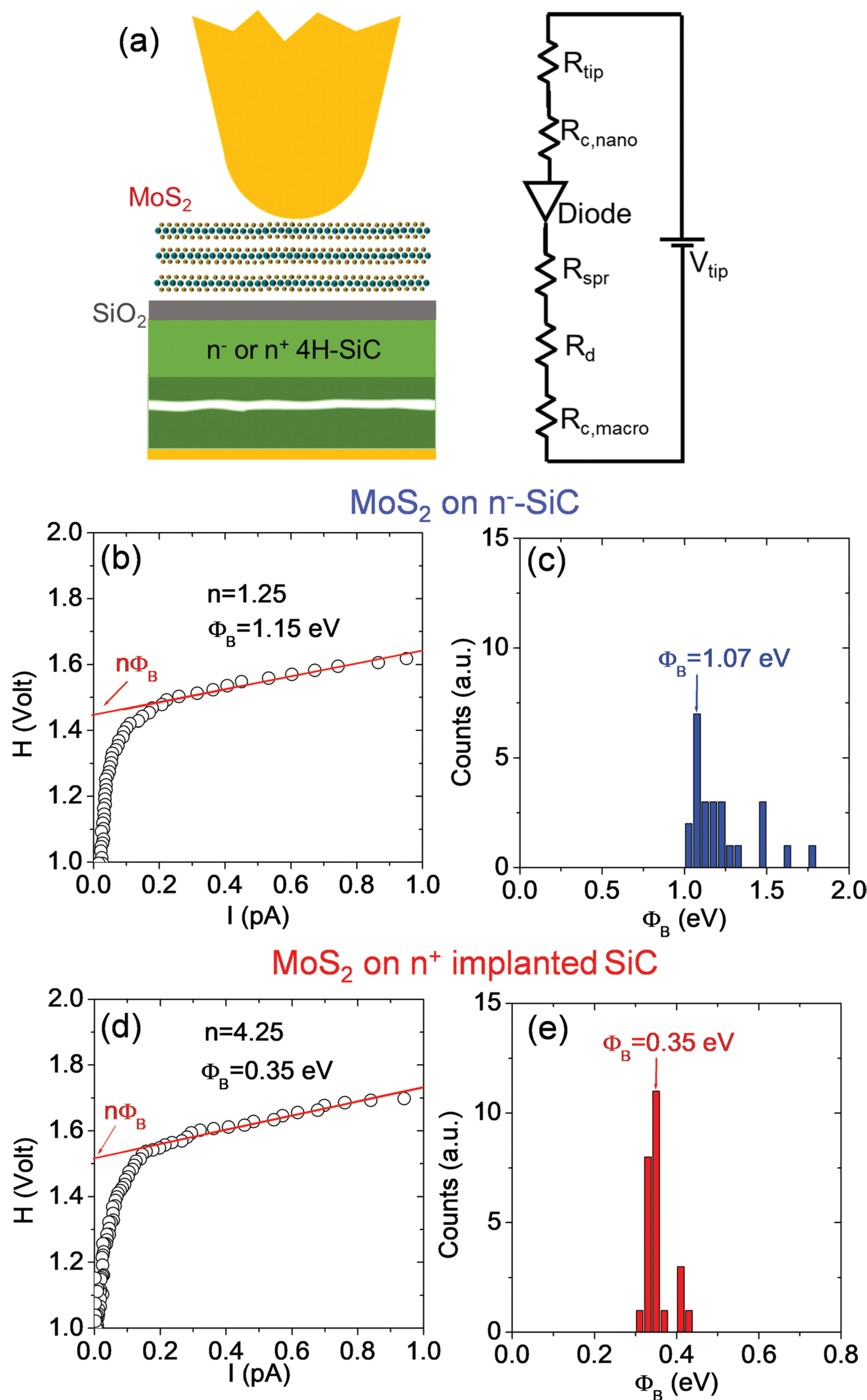

Figure 6. a) Schematic illustration of the nanoscale Pt tip contact with the MoS_2/SiC heterojunctions and its equivalent circuit. H-I plots for single tip positions on MoS_2/n^--SiC (b) and MoS_2/n^+-SiC (d), and the evaluation of the local barrier height values Φ_B. Histograms of the local Φ_B values obtained from *H–I* plots on arrays of 5 × 5 tip positions on MoS_2 on n^--SiC (c) and MoS_2 on n^+-SiC (e).

© 2022 The Authors. Advanced Materials Interfaces published by Wiley-VCH GmbH

21967350, 0, Downloaded from https://onlinelibrary.wiley.com/doi/10.1002/admi.202201502 by Cochrane Hungary, Wiley Online Library on [04/01/2023]. See the Terms and Conditions (https://onlinelibrary.wiley.com/terms-and-conditions) on Wiley Online Library for rules of use; OA articles are governed by the applicable Creative Commons License

21967350, 0, Downloaded from https://onlinelibrary.wiley.com/doi/10.1002/admi.202201502 by Cochrane Hungary, Wiley Online Library on [04/01/2023]. See the Terms and Conditions (https://onlinelibrary.wiley.com/terms-and-conditions) on Wiley Online Library for rules of use; OA articles are governed by the applicable Creative Commons License

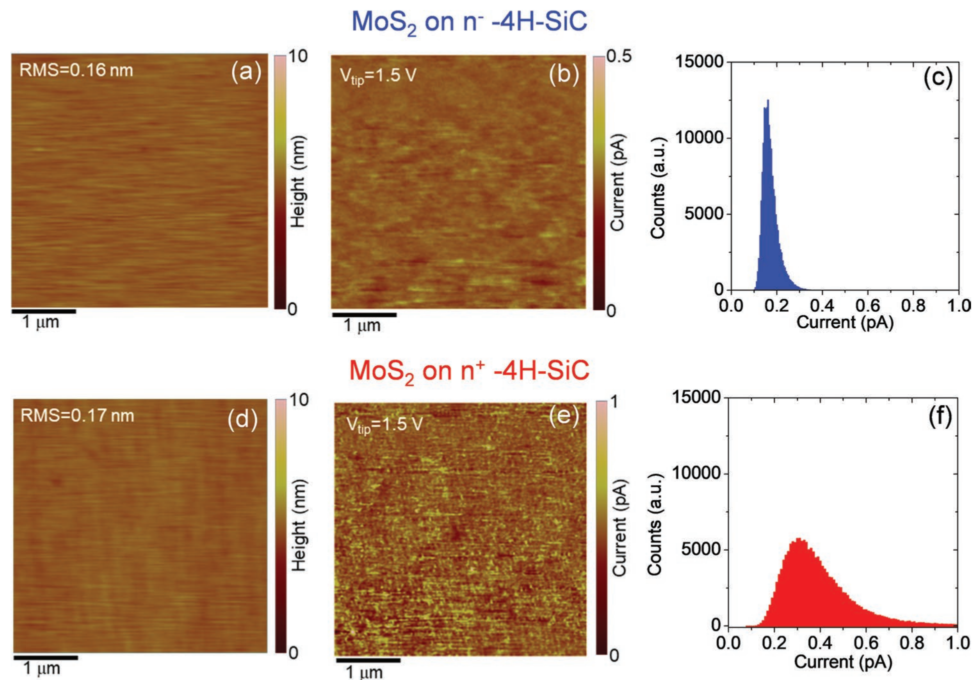

Figure 7. Surface morphology (a) and corresponding current map (b) obtained scanning the Pt tip on MoS_2 on n⁻ 4H-SiC, while applying a bias V_{tip} = 1.5 V with respect to the sample backside. Topography (d) and current map (e) collected under the same conditions for MoS_2 on n^+ 4H-SiC. c,f) Histograms of the current values extracted from the two current maps.

Due to the nanoscale tip contact size, the series resistance term $R \approx R_{C,nano}+R_{spr}$ significantly affects the $I–V_{tip}$ characteristics measured by C-AFM measured current. Hence, to account for this resistive term, the Equations. (2) and (3) have been modified as follows:

$$I = A_{tip} A^* P_t T^2 e^{-\frac{q\Phi_B}{k_B T}} e^{\frac{q(V_{tip}-IR)}{nk_B T}} \quad (8)$$

where $A_{tip} = \pi r_{tip}^2$ is the tip contact area, with $r_{tip} \approx 5$ nm.

To evaluate the local barrier height value, Equation (8) has been linearized and arranged as:

$$H = n\Phi_B + IR \quad (9)$$

where the H function is defined as[47]:

$$H = V_{tip} - \frac{nk_B T}{q} ln\left(\frac{I}{A_{tip} A^* P_t T^2}\right) \quad (10)$$

Figure 6b,d shows two H-I plots obtained from local *I–V* curves measured by the C-AFM tip on the MoS_2/n^- SiC (b) and MoS_2/n^+ SiC (d) heterojunctions, respectively. Here, the ideality factor values (n = 1.25 and n = 4.25) extracted from macroscopic *I–V* measurements at 300 K (Figure 4d) have been used for the two samples. In Figure 6b,d, the local barrier height values (Φ_B = 1.15 eV and Φ_B = 0.35 eV for the MoS_2/n^- SiC and the MoS_2/n^+ SiC junctions, respectively) were obtained according to Equation (9) by the intercept of the linear fits of the *H–I* curves on the vertical axis. Furthermore, the slopes of the fits indicate similar values of the local series resistance (R≈200 GΩ) for the two samples.

Finally, Figure 6c,e shows the histograms of the local Φ_B values obtained from *H–I* plots on arrays of 5 × 5 tip positions on MoS_2 on n^--SiC and MoS_2 on n^+-SiC, respectively. The peak values of these distributions (Φ_B = 1.07 eV and Φ_B = 0.35 eV) are in good agreement with the barrier height values obtained from temperature-dependent *I–V* analyses on macroscopic diodes (Figure 4c).

Besides local *I–V* characteristics, current mapping has been carried out using C-AFM, by scanning the metal tip on MoS_2 surface, while applying a dc bias with respect to the back contact. **Figure 7**a,b shows the surface morphology and corresponding current map obtained by scanning the Pt tip on the MoS_2/n^--SiC sample, while applying a positive bias (V_{tip} = 1.5 V) with respect to the sample backside. The topography and current map collected under the same conditions for the MoS_2 on n^+-SiC are reported in Figure 7d,e. Furthermore, the histograms of the current values extracted from the two current maps are reported in Figure 7c,f. While similar and low surface roughness (RMS = 0.16 and 0.17 nm) is measured for both samples, MoS_2 on n⁻ 4H-SiC exhibits a more uniform injected current distribution as compared to MoS_2 on n^+ 4H-SiC, as clearly demonstrated by the different shapes of the two histograms. In fact, for the first sample (Figure 7c) the histogram is more symmetric, with the peak at lower current and a short tail at higher current values. On the other hand, the histogram for the second sample exhibits the peak at a higher current and is much broader, with a longer tail at high current values. This tail is associated with the high current spots visible in the current map. These differences in the current distributions cannot be due to a different quality (e.g., defects

© 2022 The Authors. Advanced Materials Interfaces published by Wiley-VCH GmbH

density) of the MoS_2 layers, since they have been grown under identical PLD conditions on the differently doped 4H-SiC samples. On the other hand, these can be explained by the different local barrier height distributions reported in Figure 6c,e. In fact, the higher values of Φ_B for the MoS_2/n^--SiC heterojunction gives rise to lower injected current by thermionic emission above the barrier. On the other hand, in the case of MoS_2 on n^+- implanted SiC, the lower values of Φ_B and the reduced SiC depletion region give rise to larger injected current by a thermionic-field-emission mechanism. Furthermore, the nanoscale variations of the barrier height (Figure 6e) and of the SiC depletion region thickness can give rise to the significant local variation of tunneling current, i.e., to the high current spots in the current map (Figure 7e).

4. Conclusions

In conclusion, highly uniform MoS_2 films have been obtained by PLD on n^-- and on n^+-implanted 4H-SiC. Raman mapping with large statistics revealed an excellent thickness uniformity (≈3L MoS_2) and low compressive strain (0.34–0.39%) of the PLD-grown films. Atomic resolution TEM analyses showed highly conformal coverage of MoS_2 on the 4°-off SiC surface, with the presence of an ultra-thin uniform SiO_2 layer at the interface, and an excellent crystallinity of near interface 4H-SiC, even for n^+-implanted SiC. Current–voltage (*I–V*) characterizations on macroscopic diodes with patterned metal contacts and by nanoscale C-AFM measurements demonstrated a wide tunability of current injection at the hetero-interfaces by the near-surface doping of SiC, showing highly rectifying behavior on n^- 4H-SiC and strongly enhanced reverse current on n^+-implanted 4H-SiC. Finally, the mechanisms of current transport in these heterojunctions have been deeply investigated by temperature-dependent forward *I–V* characterizations, combined to nanoscale resolution C-AFM current mapping. Thermionic emission was shown to rule electron injection in MoS_2 on n^- 4H-SiC, with an effective barrier Φ_B = (1.04 ± 0.09) eV, corresponding to the MoS_2/SiC conduction band discontinuity, and temperature independent ideality factor (n ≈ 1.25) slightly departing from unity, due to a low density of interface traps between the ultra-thin SiO_2 and SiC. On the other hand, the significantly lower effective barrier Φ_B = (031 ± 0.01) eV and a temperature-dependent ideality factor n was explained by a thermionic-field-emission mechanism, with tunneling through the thin depletion region of n^+-implanted 4H-SiC. The wide tunability of electronic transport in MoS_2/SiC heterojunctions by SiC doping can be exploited in advanced or novel electronic device structures for energy efficient and fast switching applications.

Supporting Information

Supporting Information is available from the Wiley Online Library or from the author.

Acknowledgements

S. Di Franco (CNR-IMM, Catania) was acknowledged for the expert technical assistance with sample preparation. M. Vivona and R. Lo Nigro (CNR-IMM, Catania), F. M. Gelardi (Univ. of Palermo), Y. Cordier, A. Michon and M. Al Khalfioui (CNRS-CRHEA, France) are acknowledged for useful discussions. This work was funded, in part, by MUR in the framework of the FlagERA-JTC 2019 project ETMOS. Funding from CNR/SAS bilateral project PULSE and from CNR/HAS bilateral project GHOST-II for traveling in acknowledged. B.P. and A.K. acknowledged funding from the national projects TKP2021-NKTA-05 and NKFIH K_134 258. Part of the experiments was carried out using the facilities of the Italian Infrastructure Beyond Nano.

Open Access Funding provided by Consiglio Nazionale delle Ricerche within the CRUI-CARE Agreement.

Conflict of Interest

The authors declare no conflict of interest.

Data Availability Statement

The data that support the findings of this study are available from the corresponding author upon reasonable request.

Keywords

conductive atomic force microscopy, heterojunction diodes, MoS_2, pulsed laser deposition, silicon carbide

Received: July 8, 2022
Revised: August 20, 2022
Published online:

[1] S. Manzeli, D. Ovchinnikov, D. Pasquier, O. V. Yazyev, A. Kis, *Nat. Rev. Mater.* **2017**, *2*, 17033.
[2] K. S. Novoselov, O. A. Mishchenko, O. A. Carvalho, A. H. Castro Neto, *Science* **2016**, *353*, aac9439.
[3] F. Giannazzo, G. Greco, F. Roccaforte, S. S. Sonde, *Crystals* **2018**, *8*, 70.
[4] D. Jariwala, T. J. Marks, M. C. Hersam, *Nat. Mater.* **2017**, *16*, 170.
[5] P. Wang, C. Jia, Y. Huang, X. Duan, *Matter* **2021**, *4*, 552.
[6] C.-Y. Huang, C. Chang, G.-Z. Lu, W.-C. Huang, C.-S. Huang, M.-L. Chen, T.-N. Lin, J.-L. Shen, T.-Y. Lin, *Appl. Phys. Lett.* **2018**, *112*, 233106.
[7] R. Zhuo, Y. Wang, D. Wu, Z. Lou, Z. Shi, T. Xu, Y. Tian, X. Li, *J. Mater. Chem. C* **2018**, *6*, 299.
[8] Y. Wu, Z. Li, K.-W. Ang, Y. Jia, Z. Shi, Z. Huang, W. Yu, X. Sun, X. Liu, D. Li, *Photonics Res.* **2019**, *7*, 1127.
[9] M. Moun, R. Singh, *J. Appl. Phys.* **2020**, *127*, 135702.
[10] S. K. Jain, R. R. Kumar, N. Aggarwal, P. Vashishtha, L. Goswami, S. Kuriakose, A. Pandey, M. Bhaskaran, S. Walia, G. Gupta, *ACS Appl Electron Mater* **2020**, *2*, 710.
[11] Y. Xiao, L. Min, X. Liu, W. Liu, U. Younis, T. Peng, X. Kang, X. Wu, S. Ding, D. W. Zhang, *Nanophotonics* **2020**, *9*, 3035.
[12] E. W. Lee, II, C. H. Lee, P. K. Paul, L. Ma, W. D. McCulloch, S. Krishnamoorthy, Y. Wu, A. R. Arehart, S. Rajan, *Appl. Phys. Lett.* **2015**, *107*, 103505.
[13] S. Krishnamoorthy, E. W. Lee, C. H. Lee, Y. W. Zhang, W. D. McCulloch, J. M. Johnson, J. Hwang, Y. Y. Wu, S. Rajan, *Appl. Phys. Lett.* **2016**, *109*, 183505.
[14] D. Ruzmetov, K. Zhang, G. Stan, B. Kalanyan, G. R. Bhimanapati, S. M. Eichfeld, R. A. Burke, P. B. Shah, T. P. O'Regan, F. J. Crowne, A. G. Birdwell, J. A. Robinson, A. V. Davydov, T. G. Ivanov, *ACS Nano* **2016**, *10*, 3580.

© 2022 The Authors. Advanced Materials Interfaces published by Wiley-VCH GmbH

21967350, 0, Downloaded from https://onlinelibrary.wiley.com/doi/10.1002/admi.202201502 by Cochrane Hungary, Wiley Online Library on [04/01/2023]. See the Terms and Conditions (https://onlinelibrary.wiley.com/terms-and-conditions) on Wiley Online Library for rules of use; OA articles are governed by the applicable Creative Commons License

[15] T. P. O'Regan, D. Ruzmetov, M. R. Neupane, R. A. Burke, A. A. Herzing, K. Zhang, A. G. Birdwell, D. E. Taylor, E. F. C. Byrd, S. D. Walck, A. V. Davydov, J. A. Robinson, T. G. Ivanov, *Appl. Phys. Lett.* **2017**, *111*, 051602.
[16] D. Ruzmetov, M. R. Neupane, A. Herzing, T. P. O'Regan, A. Mazzoni, M. L. Chin, R. A. Burke, F. J. Crowne, A. Glen Birdwell, D. E. Taylor, A. Kolmakov, K. Zhang, J. A. Robinson, A. V. Davydov, T. G. Ivanov, *2D Mater.* **2018**, *5*, 045016.
[17] E. W. LeeII, L. Ma, D. N. Nath, C. H. Lee, A. Arehart, Y. Wu, S. Rajan, *Appl. Phys. Lett.* **2014**, *105*, 203504.
[18] H. Jeong, S. Bang, H. M. Oh, H. J. Jeong, S.-J. An, G. H. Han, H. Kim, K. K. Kim, J. C. Park, Y. H. Lee, G. Lerondel, M. S. Jeong, *ACS Nano* **2015**, *9*, 10032.
[19] P. Yan, Q. Tian, G. Yang, Y. Weng, Y. Zhang, J. Wang, F. Xie, N. Lu, *RSC Adv.* **2018**, *8*, 33193.
[20] C. Liu, H. Huang, W. Choi, J. Kim, K. Jung, W. Sun, N. Tansu, W. Zhou, H. Kuo, X. Li, *ACS Appl Electron Mater* **2020**, *2*, 419.
[21] C. R. Serrao, A. M. Diamond, S.-L. Hsu, L. You, S. Gadgil, J. Clarkson, C. Carraro, R. Maboudian, C. Hu, S. Salahuddin, *Appl. Phys. Lett.* **2015**, *106*, 052101.
[22] M. Stockmeier, R. Müller, S. A. Sakwe, P. J. Wellmann, A. Magerl, *J Appl Phys* **2009**, *105*, 033511.
[23] R. Murray, B. Evans, *J. Appl. Crystallogr.* **1979**, *12*, 312.
[24] Z. Li, R. C. Bradt, *J. Appl. Phys.* **1986**, *60*, 612.
[25] D. Wu, T. Min, J. Zhou, C. Li, G. Ma, G. Lu, M. Xia, Z. Gu, *Sci. Rep.* **2017**, *7*, 15166.
[26] F. Lan, Z. Lai, Y. Xu, H. Cheng, Z. Wang, C. Qi, J. Chen, S. Zhang, *Sci. Rep.* **2016**, *6*, 31980.
[27] J. Bradford, A. Zaganelli, D. Qi, N. Zebardastan, M. Shafiei, J. MacLeod, N. Motta, *Appl. Surf. Sci.* **2021**, *552*, 149303.
[28] F. Roccaforte, P. Fiorenza, G. Greco, R. Lo Nigro, F. Giannazzo, F. Iucolano, M. Saggio, *Microelectron. Eng.* **2018**, *187–188*, 66.
[29] F. Giannazzo, S. E. Panasci, E. Schilirò, F. Roccaforte, A. Koos, M. Nemeth, B. Pécz, *Adv. Mater. Interfaces* **2022**, *9*, 2200915.
[30] F. Giannazzo, G. Greco, E. Schilirò, R. Lo Nigro, I. Deretzis, A. La Magna, F. Roccaforte, F. Iucolano, S. Ravesi, E. Frayssinet, A. Michon, Y. Cordier, *ACS Appl Electron Mater* **2019**, *1*, 2342.
[31] C. M. Torres, Y.-W. Lan, C. Zeng, J.-H. Chen, X. Kou, A. Navabi, J. Tang, M. Montazeri, J. R. Adleman, M. B. Lerner, Y.-L. Zhong, L.-J. Li, C.-D. Chen, K. L. Wang, *Nano Lett.* **2015**, *15*, 7905.
[32] M. Lanza, *Conductive Atomic Force Microscopy: Applications in Nanomaterials*, Wiley-VCH Verlag, Weinheim, Germany **2017**.
[33] F. Giannazzo, E. Schilirò, G. Greco, F. Roccaforte, *Nanomaterials* **2020**, *10*, 803.
[34] M. Spera, G. Greco, A. Severino, M. Vivona, P. Fiorenza, F. Giannazzo, F. Roccaforte, *Appl. Phys. Lett.* **2020**, *117*, 013502.
[35] M. Vivona, G. Greco, M. Spera, P. Fiorenza, F. Giannazzo, A. La Magna, F. Roccaforte, *J. Phys. D: Appl. Phys.* **2021**, *54*, 445107.
[36] C. Lee, H. Yan, L. E. Brus, T. F. Heinz, J. Hone, S. Ryu, *ACS Nano* **2010**, *4*, 2695.
[37] D. Lloyd, X. Liu, J. S. Christopher, L. Cantley, A. Wadehra, B. L. Kim, B. B. Goldberg, A. K. Swan, J. S. Bunch, *Nano Lett.* **2016**, *16*, 5836.
[38] S. E. Panasci, E. Schilirò, F. Migliore, M. Cannas, F. M. Gelardi, F. Roccaforte, F. Giannazzo, S. Agnello, *Appl. Phys. Lett.* **2021**, *119*, 093103.
[39] H. Lee, S. Deshmukh, J. Wen, V. Z. Costa, J. S. Schuder, M. Sanchez, A. S. Ichimura, E. Pop, B. Wang, A. K. M. Newaz, *ACS Appl. Mater. Interfaces* **2019**, *11*, 31543.
[40] S. M. Sze, K. K. Ng, *Physics of Semiconductor Devices*, 3rd ed., John Wiley & Sons, Hoboken, New Jersey **2007**.
[41] F. Roccaforte, F. L.a Via, V. Raineri, R. Pierobon, E. Zanoni, *J. Appl. Phys.* **2003**, *93*, 9137.
[42] V. V. Afanasev, M. Bassler, G. Pensl, M. J. Schulz, E. Stein von Kamienski, *J. Appl. Phys.* **1996**, *79*, 3108.
[43] M. Lenzlinger, E. H. Snow, *J. Appl. Phys.* **1969**, *40*, 278.
[44] S. Y. Davydov, *Semiconductors* **2007**, *41*, 696.
[45] H. C. Card, E. H. Rhoderick, *J. Phys. D: Appl. Phys.* **1971**, *4*, 1589.
[46] G. Greco, P. Fiorenza, M. Spera, F. Giannazzo, F. Roccaforte, *J. Appl. Phys.* **2021**, *129*, 234501.
[47] S. K. Cheung, N. W. Cheung, *Appl. Phys. Lett.* **1986**, *49*, 85.

© 2022 The Authors. Advanced Materials Interfaces published by Wiley-VCH GmbH

21967350, 0, Downloaded from https://onlinelibrary.wiley.com/doi/10.1002/admi.202201502 by Cochrane Hungary, Wiley Online Library on [04/01/2023]. See the Terms and Conditions (https://onlinelibrary.wiley.com/terms-and-conditions) on Wiley Online Library for rules of use; OA articles are governed by the applicable Creative Commons License